nature physics

LETTERS

https://doi.org/10.1038/s41567-022-01703-y

Check for updates

Excitonic insulator in a heterojunction moiré superlattice

Dongxue Chen[1,2,11], Zhen Lian[1,11], Xiong Huang[3,4,11], Ying Su[5,11], Mina Rashetnia[3], Lei Ma[1], Li Yan[1], Mark Blei[6], Li Xiang[7], Takashi Taniguchi[8], Kenji Watanabe[9], Sefaattin Tongay[6], Dmitry Smirnov[7], Zenghui Wang[2]✉, Chuanwei Zhang[5]✉, Yong-Tao Cui[3]✉ and Su-Fei Shi[1,10]✉

Two-dimensional moiré superlattices provide a highly tunable platform to study strongly correlated physics. In particular, the moiré superlattices of two-dimensional semiconductor heterojunctions have been shown to host tunable correlated electronic states such as a Mott insulator and generalized Wigner crystals[1-4]. Here we report the observation of an excitonic insulator[5-7], a correlated state with strongly bound electrons and holes, in an angle-aligned monolayer WS_2/bilayer WSe_2 moiré superlattice. The moiré coupling induces a flat miniband on the valence-band side only in the first WSe_2 layer interfacing WS_2. The electrostatically introduced holes first fill this miniband and form a Mott insulator when the carrier density corresponds to one hole per moiré supercell. By applying a vertical electric field, we tune the valence band in the second WSe_2 layer to overlap with the moiré miniband in the first WSe_2 layer, realizing the coexistence of electrons and holes at equilibrium, which are bound as excitons due to a strong Coulomb interaction. We show that this new bound state is an excitonic insulator with a transition temperature as high as 90 K. Our study demonstrates a moiré system for the study of correlated many-body physics in two dimensions.

An excitonic insulator (EI) is a bound state of electron and hole pairs due to a strong Coulomb interaction[5–7]. Motivated by its relevance to Bose–Einstein condensation, researchers have long been looking for this exotic quantum state, although the study is often hindered by low transition temperatures or elusive experimental signatures. Recently, two-dimensional moiré superlattices have emerged as a controllable material platform with a strong Coulomb interaction[8], which has led to the discovery of a variety of novel quantum phases such as superconductor, Mott insulator and correlated Chern insulator[1–4,9–20]. The strong electronic correlation in moiré superlattices is enabled by the formation of flat minibands in which the kinetic energy of charge carriers is substantially reduced. Meanwhile, owing to their small bandwidth, these minibands make it possible to realize the coexistence of electrons and holes via band engineering, a prerequisite to form EIs. The strong Coulomb interaction further provides the glue for the strong binding of electron–hole pairs. In this work, we explore the possibility of EI in the highly tunable moiré superlattice of angle-aligned transition metal dichalcogenides (TMDCs), which has been shown to exhibit particularly strong electron correlation, evidenced by the Mott insulator state with high transition temperatures and various correlated insulating states at fractional fillings of the moiré superlattice[1,2,4].

In this work, we study the moiré superlattice of angle-aligned monolayer WS_2/bilayer WSe_2 (1L/2L WS_2/WSe_2). We focus on the hole-doping regime as the valence band of TMDC heterobilayers has been readily modelled for the study of a single-band Hubbard model[20]. In WS_2/WSe_2 heterojunctions, the holes reside in the WSe_2 layers due to the type-II alignment[21], and it has been demonstrated that moiré coupling in monolayer WS_2/monolayer WSe_2 (1L/1L WS_2/WSe_2) forms a flat miniband in WSe_2 that enables the Mott insulator state at $n=-1$, one hole per moiré unit cell. In the 1L/2L WS_2/WSe_2 moiré superlattice studied here, the second WSe_2 layer in the natural bilayer WSe_2, away from the WS_2/WSe_2 interface, contributes a parabolic valence band (VB2) that is energetically close to the moiré miniband (MB1) in the first WSe_2 layer at the interface (Fig. 1e). By applying an out-of-plane electric field, these two bands can overlap in energy, and electrostatic doping can be used to simultaneously populate electron-like carriers in MB1 and hole-like carriers in VB2 (Fig. 1f), experimentally revealed by the optical signatures of exciton–polarons from the second WSe_2 layer. Using microwave impedance microscopy (MIM), we further find that the system goes into an insulating state at $n=-1$, at which the electron density in MB1 is equal to the hole density in VB2, confirming that these electrons and holes form a strongly bound EI state. This EI state is robust and exhibits a transition temperature as high as 90 K.

As shown in the schematic in Fig. 1a, a typical device consists of a monolayer WS_2 angle aligned on top of a natural bilayer WSe_2, and the heterojunction is encapsulated with boron nitride (BN) flakes. The 1L/2L WS_2/WSe_2 heterostructure (with the former layer on top) is dual gated by few-layer graphene (FLG) electrodes on both top and bottom, which allows us to independently control the doping density n and electric field E (Methods). The optical microscopy image of device D1 is shown in Extended Data Fig. 1.

We first investigate the optical signatures of the dual-gate 1L/2L WS_2/WSe_2 heterojunction. Moiré coupling in the TMDC heterojunction has been shown to strongly modify the excitonic behaviours[22–25]. Here we study the moiré effect on the exciton through the optical reflectance spectra as a function of carrier density with electric field $E=0$ (Fig. 1b). The reflectance spectra are distinctively

[1]Department of Chemical and Biological Engineering, Rensselaer Polytechnic Institute, Troy, NY, USA. [2]Institute of Fundamental and Frontier Sciences, University of Electronic Science and Technology of China, Chengdu, China. [3]Department of Physics and Astronomy, University of California, Riverside, CA, USA. [4]Department of Materials Science and Engineering, University of California, Riverside, CA, USA. [5]Department of Physics, University of Texas at Dallas, Dallas, TX, USA. [6]School for Engineering of Matter, Transport and Energy, Arizona State University, Tempe, AZ, USA. [7]National High Magnetic Field Lab, Tallahassee, FL, USA. [8]International Center for Materials Nanoarchitectonics, National Institute for Materials Science, Tsukuba, Japan. [9]Research Center for Functional Materials, National Institute for Materials Science, Tsukuba, Japan. [10]Department of Electrical, Computer & Systems Engineering, Rensselaer Polytechnic Institute, Troy, NY, USA. [11]These authors contributed equally: Dongxue Chen, Zhen Lian, Xiong Huang, Ying Su. ✉e-mail: zenghui.wang@uestc.edu.cn; Chuanwei.Zhang@utdallas.edu; yongtao.cui@ucr.edu; shis2@rpi.edu

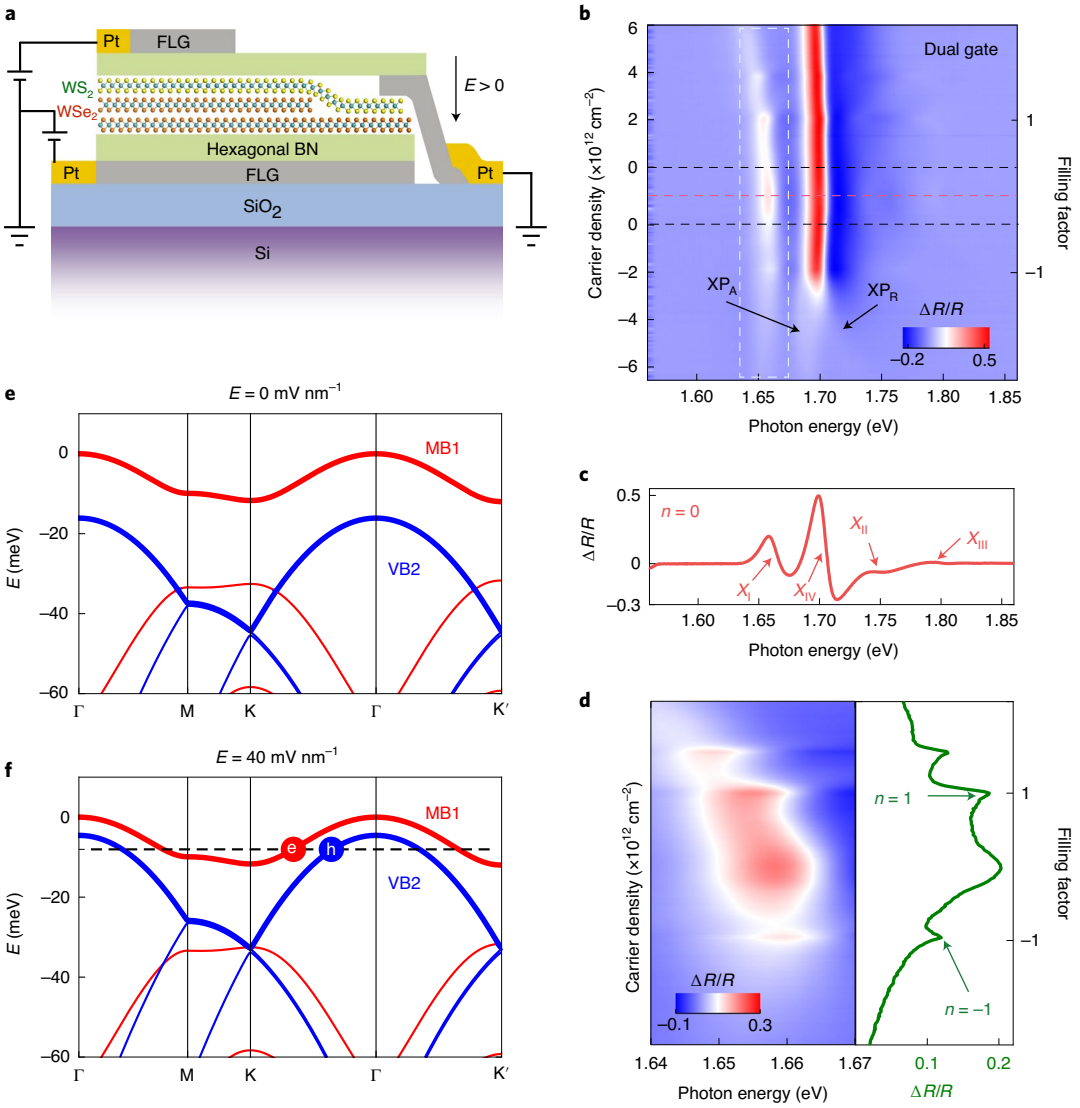

Fig. 1 | Moiré superlattice of 1L/2L WS_2/WSe_2. **a**, Schematic of angle-aligned 1L/2L WS_2/WSe_2 heterojunction device D1. **b**, Optical reflectance spectra as a function of carrier density (filling factor) for zero vertical electric field $E = 0$ at 5 K. The charge-neutral region is indicated by the black dashed lines (region in which moiré excitons X_{II} and X_{III} are visible). **c**, Linecut of the optical spectra in **b** at charge neutrality $n = 0$. **d**, Zoomed-in view of the white-box region in **b** (left) and the peak intensity (right). **e**,**f**, Calculations of the valence bands for the cases of $E = 0$ (**e**) and $E = 40\,\mathrm{mV\,nm^{-1}}$ (**f**). MB1 is the flat miniband from the first WSe_2 layer due to the moiré coupling and VB2 is the valence band from the second WSe_2 layer. When the Fermi level crosses both MB1 and VB2, carriers are electron-like in MB1 but hole-like in VB2.

different from that of the 1L/1L WS_2/WSe_2 moiré superlattice studied previously[24]. In 1L/1L WS_2/WSe_2, the A-exciton resonance of WSe_2 is split into three moiré exciton peaks, whereas in 1L/2L WS_2/WSe_2, there are four exciton peaks when the system is charge neutral. The peaks X_I, X_{II} and X_{III} are located at ~1.665, 1.747 and 1.798 eV, respectively, whereas X_{IV} is located at ~1.705 eV and close to the original A-exciton resonance of WSe_2 (Fig. 1c). These four exciton peaks are similar for all the angle-aligned 1L/2L WS_2/WSe_2 devices studied here. They can be explained by the interfacial nature of the moiré coupling between WSe_2 and WS_2. The A exciton of the first WSe_2 layer (the one interfacing WS_2) is split into three moiré exciton peaks (X_I, X_{II} and X_{III}), similar to the case of the 1L/1L WS_2/WSe_2 moiré superlattice. The second WSe_2 layer away from the WS_2/WSe_2 interface, however, is not strongly affected by the moiré coupling because interlayer hopping in bilayer WSe_2 is virtually suppressed by the AB-stacking pattern and the layer is approximately a good quantum number. This interpretation is supported by our numerical results (Fig. 1e) in which the moiré minibands from the first and second WSe_2 layers are marked by red and blue colours, respectively. The moiré coupling hybridizes adjacent minibands at the moiré Brillouin-zone boundary (Fig. 1e, the M to K segment) at which the original energy bands of the constituent WSe_2 layers are folded back. The level repulsion at the zone boundary manifests the strength of moiré coupling, which is strong in the first WSe_2 layer and gives rise to the flat minibands. On the other hand, the minibands in the second WSe_2 layer remain nearly degenerate at the zone boundary, suggesting that the moiré coupling has a small effect. Therefore, the intralayer A-exciton resonance in the second WSe_2 layer remains at roughly the same energy and corresponds to the observed X_{IV} peak.

The moiré exciton at the lowest energy, X_I, is sensitive to the carrier density and exhibits intensity resonances at an electron or hole density of about $2.0 \times 10^{12}\,\mathrm{cm^{-2}}$, which corresponds to filling factor of $n = 1$ (one electron per moiré unit cell) and -1 (one hole

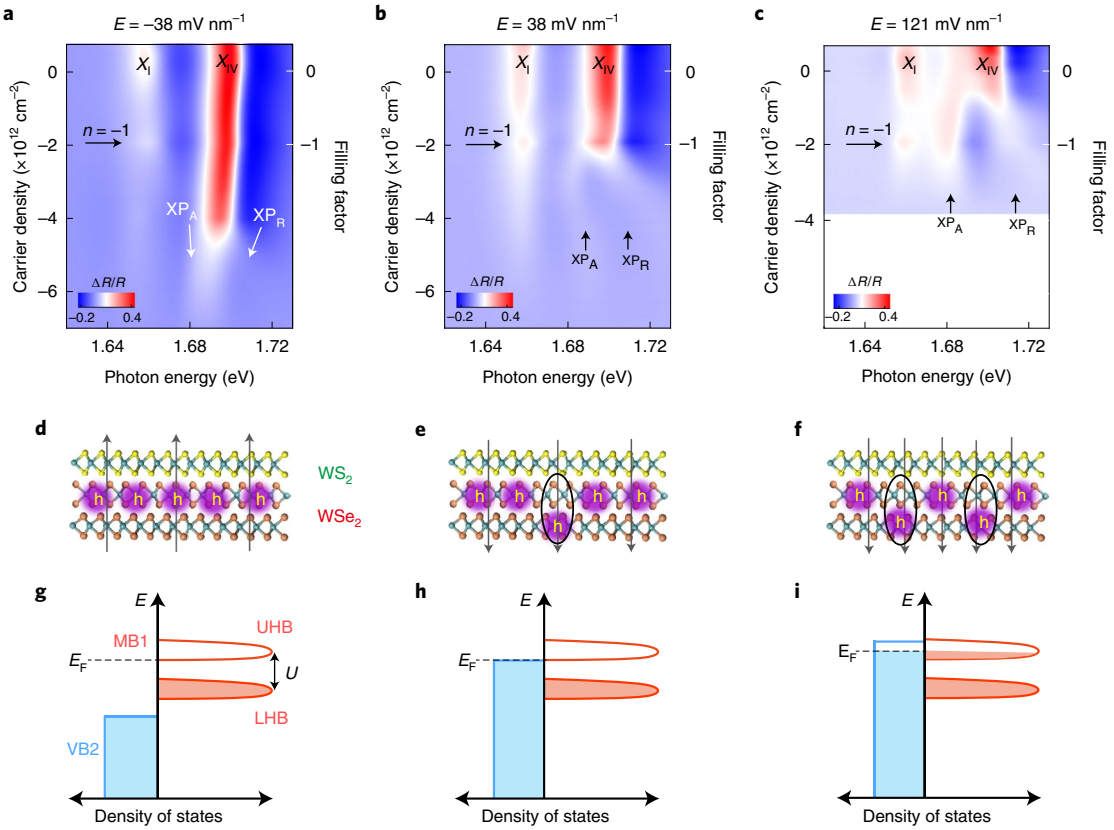

Fig. 2 | Electric-field tuning of the band alignment in dual-gate 1L/2L WS_2/WSe_2. a–c, Doping dependence of the optical reflectance spectra at electric fields of -38 mV nm^{-1} (**a**), 38 mV nm^{-1} (**b**) and 121 mV nm^{-1} (**c**). **d–f**, Schematic of the distribution of holes in the two WSe_2 layers for **a–c** (**d–f**, respectively), where the ellipse denotes the interlayer exciton formed by the hole transferred to the second layer of WSe_2 and electron left behind in the first layer of WSe_2. **g–i**, Schematic of the valence-band alignment at total filling $n=-1$ corresponding to **a–c** (**g–i**, respectively). At $n=-1$, the flat MB1 is split into LHB and UHB. The relative alignment between VB2 and MB1 is tuned by the electric field.

per moiré unit cell) (Fig. 1d). This behaviour is likely due to the reduced screening associated with the formation of insulating states (Fig. 3, MIM measurements), similar to the case of 1L/1L WSe_2/WS_2 moiré superlattice[1,2,4,21]. It is worth noting that at $n=-1$, moiré exciton X_{IV} remains the same as that in charge-neural doping ($n=0$). However, X_{IV} splits into an attractive exciton–polaron (XP_A) and a repulsive exciton–polaron (XP_R) at increased doping at around $n=-1.5$ (total hole density of about 3.0×10^{12} cm^{-2}). The exciton–polaron in TMDCs arises from the many-body interaction between the intralayer exciton and free carriers, with the exciton interacting with the Fermi sea of the opposite (same) valley leading to the redshifted (blueshifted) attractive (repulsive) exciton–polaron[26–29]. The doping dependence of X_{IV}, therefore, suggests that at $n=-1$, all the holes reside in the first WSe_2 layer, and they start to fill the second WSe_2 layer at n of about −1.5 for the $E=0$ case. This observation inspires us to apply a vertical electric field to engineer the relative alignment of MB1 and VB2, which could allow holes to populate the second WSe_2 layer at a much lower hole doping ($-1<n<0$). This is feasible according to our calculation (Fig. 1f), in which a positive electric field (pointing from WS_2 towards WSe_2) moves VB2 up relative to MB1. When E is large enough, VB2 can overlap with the flat MB1, which allows carriers to transfer from the first WSe_2 layer to the second WSe_2 layer. When the total doping is at a level such that both MB1 and VB2 are partially filled, that is, the Fermi level lies in the overlap range, the carriers near the Fermi level in MB1 are electron-like due to the positive band curvature near the bottom of the band. On the other hand, the carriers in VB2 are hole-like as they are near the top of the valence band. This band alignment creates an interesting scenario in which electrons and holes can simultaneously exist but in different WSe_2 layers, setting up the stage for the formation of an EI.

We next experimentally demonstrate the coexistence of electrons and holes in separate WSe_2 layers by using an electric field to tune the band alignment. For each specific electric field, we measure the doping dependence of the optical reflectance spectra: the data for three characteristic electric fields are shown in Fig. 2 (Extended Data Fig. 2 provides more data for different electric fields). For all the three cases, moiré exciton X_I exhibits a resonance at a hole density of about 2.0×10^{12} cm^{-2}, corresponding to a total filling level of $n=-1$. However, moiré exciton X_{IV}, which arises from the A-exciton response of the second WSe_2 layer, shows different behaviours at different electric fields. At $E=-38$ mV nm^{-1}, the splitting of X_{IV} into two exciton–polarons, namely, XP_A and XP_R, occurs at a high-hole-doping level corresponding to n of about −2.3. Before reaching this doping level, all the carriers should be in MB1. Therefore, the $n=-1$ state should correspond to the Mott insulator state at the half-filling of MB1 with one hole per moiré unit cell. The strong on-site Coulomb repulsion splits the originally doubly degenerate MB1 into a lower Hubbard band (LHB) and an upper Hubbard band (UHB). For $n=-1$, the Fermi level lies just below the UHB (Fig. 2g). VB2, which starts to be filled at n of about −2.3, should lie even below the LHB, consistent with the negative direction of the electric field that pushes holes to the first WSe_2 layer (Fig. 2d). Under a positive electric field that moves VB2 up, the onset of the exciton–polaron is expected to occur at a lower hole doping. We find that at $E=38$ mV nm^{-1}, this onset occurs at roughly $n=-1$ (Fig. 2b).

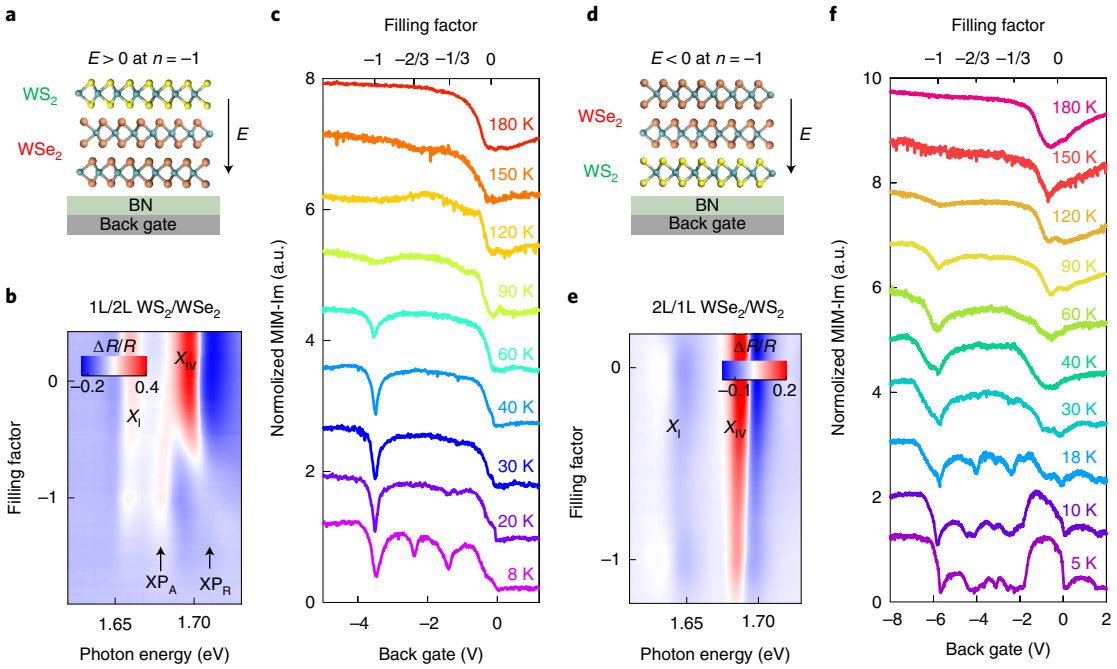

Fig. 3 | MIM spectra of single-gate 1L/2L WS_2/WSe_2 devices with opposite stacking orders. a, Schematic of single-gate 1L/2L WS_2/WSe_2 devices. **b**,**c**, Optical (**b**) and MIM (**c**) spectra as a function of hole doping for the single-gate 1L/2L WS_2/WSe_2 region in device D1. **d**, Schematic of single-gate 2L/1L WSe_2/WS_2 devices. **e**,**f**, Doping-dependent optical (**e**) and MIM (**f**) spectra for the 2L/1L WSe_2/WS_2 regions in device D5. The arrows in **a** and **d** denote the electric-field direction at $n=-1$.

This suggests that the band maximum of VB2 is at the same energy level as the bottom of the UHB of MB1 (Fig. 2h). The Fermi level at $n=-1$ should now touch both bottom of LHB and top of VB2. As the electric field further increases, these two bands start to overlap; when the total doping level is fixed at $n=-1$, some carriers now transfer from the UHB to VB2 (Fig. 2e,f). From the perspective of electron-like carriers, the electron density in the UHB of MB1 (n_e) is exactly the same as the hole density in VB2 (n_h), that is, $n_e=n_h$. The case of $E=121\,\mathrm{mV\,nm^{-1}}$ is such an example. The onset of exciton–polaron clearly occurs at a lower hole doping than $n=-1$ (Fig. 2c). Therefore, the $n=-1$ state corresponds to a state with coexisting electrons in MB1 and holes in VB2 of equal densities—a potential candidate for an EI.

The remaining step is to show that this state is insulating, which we demonstrate by combining MIM and optical spectroscopy measurements. MIM measures the local conductivity in a small sample area (~100 nm) underneath the tip. We have fabricated three types of device: (1) 1L/2L WS_2/WSe_2 with only a single back graphite gate (Fig. 3a); (2) an inverted stack with 2L WSe_2 on the top of 1L WS_2, that is, 2L/1L WSe_2/WS_2, with a single bottom graphite gate (Fig. 3d); (3) dual-gate devices with a monolayer graphene as the top gate (Extended Data Fig. 3a). All three types of device show consistent behaviours. Since the layer stacking order is opposite in type-1 and type-2 devices, the electric-field directions are also opposite (Fig. 2) when the total carrier density is tuned to $n=-1$ by the back gate (Fig. 3a,d). In the 1L/2L WS_2/WSe_2 (type-1) device, the electric field is positive at around $n=-1$, and the optical reflectance measurement indicates that the holes reside on both layers of 2L WSe_2 (Fig. 3b). The gate dependence of MIM in this device clearly shows an insulating state at $n=-1$. These results, thus, confirm the existence of the EI state in the 1L/2L WS_2/WSe_2 device. This EI state has a transition temperature of around 90 K, determined from the temperature dependence of the MIM spectra (Fig. 3c). As a comparison, the 2L/1L WSe_2/WS_2 (type-2) device exhibits a Mott insulator state at $n=-1$ since the corresponding electric field is negative and pushes all the holes to the first WSe_2 layer, which is confirmed by the optical reflectance measurement (Fig. 3e). The Mott insulator state has a transition temperature of around 120 K, as determined from the MIM results (Fig. 3f). The different transition temperatures reflect the different characteristics of the EI and Mott insulator states, both at $n=-1$. As a control experiment, the 1L/1L WS_2/WSe_2 regions in type-1 and type-2 devices have a similar transition temperature of around 180 K, indicating similar moiré couplings (Extended Data Fig. 4).

In a dual-gate 1L/2L WS_2/WSe_2 (type-3) device, we can realize both Mott insulator and EI state in a single device under different electric fields (Extended Data Fig. 3). At 20 K, the dual-gate MIM maps show an insulating feature at $n=-1$ in the entire accessible range of electric fields, expected for both Mott insulator and EI states. The difference between the two insulating states can be shown in their temperature dependence: at 70 K, the EI state disappears whereas the Mott insulator state persists. This difference arises from the strength of the Coulomb interaction associated with these states and is consistent with the data in Fig. 3. A detailed analysis of Extended Data Fig. 3 can be found in the Supplementary Information.

Finally, we use helicity-resolved magnetoreflectance spectroscopy to further confirm the exciton–polarons and the correlation of holes from the first and second layer of WSe_2 in the EI state. The exciton–polarons arise from the interaction between the intralayer exciton and carriers in the same (attractive exciton–polaron) or opposite (repulsive exciton–polaron) valley. An out-of-plane magnetic field lifts the valley degeneracy and leads to an energy difference between the valence bands from K and K' valleys. As a result, the hole doping starts to first fill one particular valley, say, the K valley, and the screening of the excitons in the opposite (K') or same (K) valley results in the attractive (repulsive) exciton–polaron[26–29]. To confirm this, we excite the device with right-circularly (left-circularly) polarized light, that is, σ^+ (σ^-), and probe the reflectance contrast in the right-circularly (left-circularly) polarized channel. The data

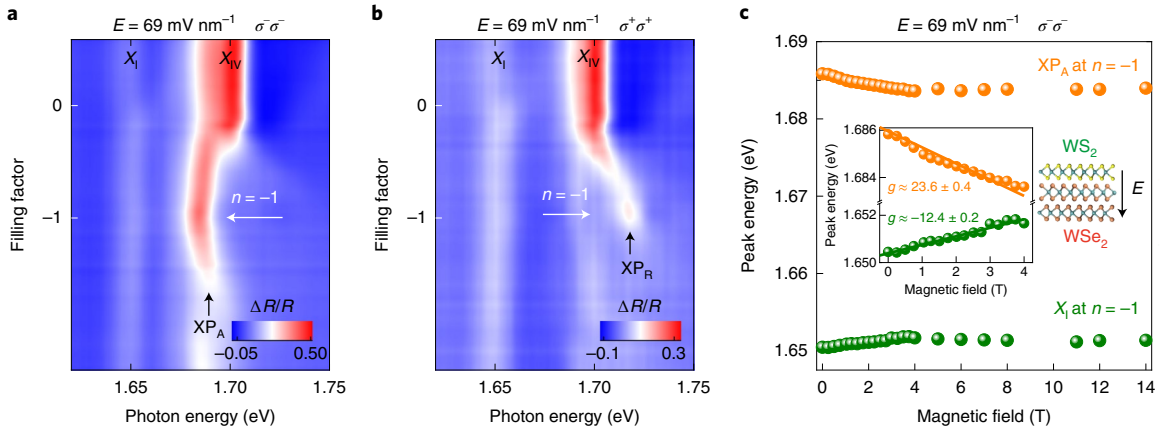

Fig. 4 | Helicity-resolved magnetoreflectance spectra under an out-of-plane magnetic field. a,**b**, Doping-dependent reflectance spectra from K′ and K valley for an angle-aligned 1L/2L WS_2/WSe_2 device (device D2) under an electric field of 69 mV nm^{-1} and magnetic field of 4 T, showing the attractive exciton–polaron (**a**) and repulsive exciton–polaron (**b**) from exciton resonance X_{IV} (near 1.70 eV). **c**, Energy of attractive exciton–polaron XP_A and moiré exciton X_I at $n=-1$ as a function of the magnetic field. The inset shows the *g*-factor obtained by fitting the Zeeman shift below the saturation field (≈4 T), along with the electric-field direction relative to the 1L/2L WS_2/WSe_2 stacking (shown as the schematic).

obtained from an out-of-plane magnetic field of 4 T are shown in Fig. 4. Under the electric field of 69 mV nm^{-1}, the 1L/2L WS_2/WSe_2 heterojunction is at the EI state, and it is obvious that the intralayer exciton from the second layer of WSe_2 (X_{IV}) behaves as an attractive exciton–polaron (Fig. 4a) in the $\sigma^-\sigma^-$ measurement configuration and repulsive exciton–polaron in the $\sigma^+\sigma^+$ configuration (Fig. 4b) at $n=-1$.

We further measure the Zeeman shifts of both XP_A and X_I at the EI state ($n=-1$; Fig. 4a). The Zeeman splitting[30] of the absorption peaks are defined by $E = E_0 \pm \frac{1}{2}g\mu_B B$, where g is the Landé *g*-factor and μ_B is the Bohr magneton. The '+' and '−' signs denote the absorption peak energies from the K and K' valleys, respectively. Both XP_A and X_I exhibit unique dependence on the magnetic field: a large Zeeman shift is observed in the relatively low magnetic-field regime, characterized by a *g*-factor much larger than 4, which then saturates at a high magnetic field. The behaviour of moiré exciton X_I at $n=-1$ has been reported previously[2], which was ascribed to the magnetic properties of the ground state of the Mott insulator[2,20] in 1L/1L WS_2/WSe_2. Here, in the EI state of the 1L/2L WS_2/WSe_2, although some holes are moved to the second layer of WSe_2, these holes are still strongly correlated magnetically with the holes in the first layer of WSe_2; therefore, the associated exciton–polaron exhibits a similar Zeeman splitting behaviour. In contrast, when 1L/2L WS_2/WSe_2 is in the Mott insulator state ($n=-1$), the X_{IV} intralayer exciton in the second WSe_2 layer shows a Zeeman splitting with a *g*-factor of about 4 (Extended Data Fig. 5). This behaviour is expected for the Mott insulator state: since all the correlated holes are confined in the first layer of WSe_2, the X_{IV} exciton is essentially the A exciton from the second layer of WSe_2, with an expected 'normal' *g*-factor of intralayer exciton of about 4.

Overall, the combined MIM and optical spectroscopy results support that the state at $n=-1$, when holes partially populate the second WSe_2 layer (Fig. 2f), is an EI state. The equal number of electrons in MB1 and holes in VB2 are tightly bound as charge-neutral excitons due to the strong Coulomb interactions considering the small physical van der Waals gap between the first and second layer of WSe_2 (~0.3 nm). Since no free carriers are left behind, and the charge-neutral excitons do not contribute to any charge transport, the system is in an insulating state. This insulating state should be rather sensitive to the imbalance of electron and hole densities, which is reflected as the width of the insulating feature in the MIM spectra (Supplementary Information). We note that the EI transition temperatures in this system are much higher than those reported in two-dimensional electron-gas-based EI systems[31,32] or the EI in bilayer graphene[33,34]. They are also higher than the EI states recently reported in a different TMDC moiré superlattice[35,36]. The robustness of the EI state originates from the strong correlation in the flat moiré miniband and the strong Coulomb interaction that leads to the tightly bound interlayer excitons across the van der Waals gap of bilayer WSe_2, which inspires further engineering of new quantum states such as superfluidity in an EI system[37].

Online content

Any methods, additional references, Nature Research reporting summaries, source data, extended data, supplementary information, acknowledgements, peer review information; details of author contributions and competing interests; and statements of data and code availability are available at https://doi.org/10.1038/s41567-022-01703-y.

Received: 16 October 2021; Accepted: 29 June 2022;
Published online: 8 August 2022

References

1. Regan, E. C. et al. Mott and generalized Wigner crystal states in WSe_2/WS_2 moiré superlattices. *Nature* **579**, 359–363 (2020).
2. Tang, Y. et al. Simulation of Hubbard model physics in WSe_2/WS_2 moiré superlattices. *Nature* **579**, 353–358 (2020).
3. Xu, Y. et al. Correlated insulating states at fractional fillings of moiré superlattices. *Nature* **587**, 214–218 (2020).
4. Huang, X. et al. Correlated insulating states at fractional fillings of the WS_2/WSe_2 moiré lattice. *Nat. Phys.* **17**, 715–719 (2021).
5. Mott, N. F. The transition to the metallic state. *Philos. Mag.* **6**, 287–309 (1961).
6. Jerome, D., Rice, T. M. & Kohn, W. Excitonic insulator. *Phys. Rev.* **158**, 462–475 (1967).
7. Halperin, B. I. & Rice, T. M. Possible anomalies at a semimetal-semiconductor transition. *Rev. Mod. Phys.* **40**, 755–766 (1968).
8. Qiu, D. Y., da Jornada, F. H. & Louie, S. G. Optical spectrum of MoS_2: many-body effects and diversity of exciton states. *Phys. Rev. Lett.* **111**, 216805 (2013).
9. Cao, Y. et al. Unconventional superconductivity in magic-angle graphene superlattices. *Nature* **556**, 43–50 (2018).
10. Cao, Y. et al. Correlated insulator behaviour at half-filling in magic-angle graphene superlattices. *Nature* **556**, 80–84 (2018).
11. Chen, G. et al. Evidence of a gate-tunable Mott insulator in a trilayer graphene moiré superlattice. *Nat. Phys.* **15**, 237–241 (2019).

12. Chen, G. et al. Signatures of tunable superconductivity in a trilayer graphene moiré superlattice. *Nature* **572**, 215–219 (2019).
13. Wang, L. et al. Correlated electronic phases in twisted bilayer transition metal dichalcogenides. *Nat. Mater.* **19**, 861–866 (2020).
14. Ghiotto, A. et al. Quantum criticality in twisted transition metal dichalcogenides. *Nature* **597**, 345–349 (2021).
15. Li, T. et al. Quantum anomalous Hall effect from intertwined moiré bands. *Nature* **600**, 641–646 (2021).
16. Zhou, Y. et al. Bilayer Wigner crystals in a transition metal dichalcogenide heterostructure. *Nature* **595**, 48–52 (2021).
17. Shimazaki, Y. et al. Strongly correlated electrons and hybrid excitons in a moiré heterostructure. *Nature* **580**, 472–477 (2020).
18. Andrei, E. Y. & MacDonald, A. H. Graphene bilayers with a twist. *Nat. Mater.* **19**, 1265–1275 (2020).
19. Balents, L., Dean, C. R., Efetov, D. K. & Young, A. F. Superconductivity and strong correlations in moiré flat bands. *Nat. Phys.* **16**, 725–733 (2020).
20. Wu, F., Lovorn, T., Tutuc, E. & MacDonald, A. H. Hubbard model physics in transition metal dichalcogenide moiré bands. *Phys. Rev. Lett.* **121**, 026402 (2018).
21. Miao, S. et al. Strong interaction between interlayer excitons and correlated electrons in WSe_2/WS_2 moiré superlattice. *Nat. Commun.* **12**, 3608 (2021).
22. Seyler, K. L. et al. Signatures of moiré-trapped valley excitons in $MoSe_2/WSe_2$ heterobilayers. *Nature* **567**, 66–70 (2019).
23. Rivera, P. et al. Interlayer valley excitons in heterobilayers of transition metal dichalcogenides. *Nat. Nanotech.* **13**, 1004–1015 (2018).
24. Jin, C. et al. Observation of moiré excitons in WSe_2/WS_2 heterostructure superlattices. *Nature* **567**, 76–80 (2019).
25. Alexeev, E. M. et al. Resonantly hybridized excitons in moiré superlattices in van der Waals heterostructures. *Nature* **567**, 81–86 (2019).
26. Efimkin, D. K. & MacDonald, A. H. Many-body theory of trion absorption features in two-dimensional semiconductors. *Phys. Rev. B* **95**, 035417 (2017).
27. Efimkin, D. K. & Macdonald, A. H. Exciton-polarons in doped semiconductors in a strong magnetic field. *Phys. Rev. B* **97**, 235432 (2018).
28. Wang, T. et al. Observation of quantized exciton energies in monolayer WSe_2 under a strong magnetic field. *Phys. Rev. X* **10**, 021024 (2020).
29. Smoleński, T. et al. Interaction-induced Shubnikov–de Haas oscillations in optical conductivity of monolayer $MoSe_2$. *Phys. Rev. Lett.* **123**, 097403 (2019).
30. Li, Z. et al. Momentum-dark intervalley exciton in monolayer tungsten diselenide brightened via chiral phonon. *ACS Nano* **13**, 14107–14113 (2019).
31. Du, L. et al. Evidence for a topological excitonic insulator in InAs/GaSb bilayers. *Nat. Commun.* **8**, 1971 (2017).
32. Eisenstein, J. P. Exciton condensation in bilayer quantum Hall systems. *Annu. Rev. Condens. Matter Phys.* **5**, 159–181 (2014).
33. Liu, X. et al. Interlayer fractional quantum Hall effect in a coupled graphene double layer. *Nat. Phys.* **15**, 893–897 (2019).
34. Li, J. I. A., Taniguchi, T., Watanabe, K., Hone, J. & Dean, C. R. Excitonic superfluid phase in double bilayer graphene. *Nat. Phys.* **13**, 751–755 (2017).
35. Zhang, Z. et al. Correlated interlayer exciton insulator in double layers of monolayer WSe_2 and moiré WS_2/WSe_2. Preprint at https://arxiv.org/abs/2108.07131 (2021).
36. Gu, J. et al. Dipolar excitonic insulator in a moiré lattice. *Nat. Phys.* **18**, 395–400 (2022).
37. Fogler, M. M., Butov, L. V. & Novoselov, K. S. High-temperature superfluidity with indirect excitons in van der Waals heterostructures. *Nat. Commun.* **5**, 4555 (2014).

Methods

Heterostructure device fabrication. We use a dry pickup method to fabricate the WS_2/WSe_2 heterostructures. We exfoliate monolayer WS_2, multilayer WSe_2, FLG and BN flakes on a silicon substrate with a 285 nm thermal oxide layer. For angle-aligned heterostructures, we choose exfoliated WS_2 and WSe_2 flakes with sharp edges, whose crystal axes are further confirmed by second-harmonic-generation measurements. We then mount the SiO_2/Si substrate on a rotational stage and clamp the glass slide with thin flakes to another three-dimensional stage. We adjust the three-dimensional stage to control the distance between the substrates and thin flakes, and we sequentially pickup different flakes onto prepatterned Pt electrodes on SiO_2/Si substrates. We finely adjust the angle of the rotational stage (accuracy of 0.02°) under a microscope objective to stack the WS_2/WSe_2 heterojunction, ensuring a near-zero twist angle between the two flakes. The final constructed device is annealed at 130 °C for 12 h in a vacuum chamber. The prepatterned Pt contact electrodes are fabricated through standard electron-beam lithography and electron-beam evaporation processes (Extended Data Fig. 1 shows the optical microscopy images of device D1). For devices D1 and D5, the heterostructure regions are partially covered by top-gate FLG flakes. MIM measurements were first performed in regions without the FLG top gate to obtain data on single-gate regions (Extended Data Fig. 3). Then, monolayer graphene flakes were transferred over these regions and used as the top gate to obtain the data shown in Fig. 3 and Supplementary Information. The twist angle between WS_2 and WSe_2 can be determined from the MIM spectra, which is $0.4° \pm 0.2°$ and $0.3° \pm 0.2°$ for the 1L/1L and 1L/2L WS_2/WSe_2 regions in device D1, respectively, as shown in the main text.

Optical spectroscopy measurements. To perform differential reflectance contrast measurements, the samples were mounted in a helium flow-controlled cryostat with a quartz optical window and electrical feedthroughs. A super-continuum laser (YSL Photonics) was used as the white-light source. The laser was focused onto the sample with a ×50 objective (the typical laser spot size is ~2 μm). The reflected light was directed into a spectrograph and collected with a charge-coupled device camera (Princeton Instruments). The differential reflectance is calculated as $\frac{\Delta R}{R} = \frac{R-R_0}{R_0}$ by using the reflectance spectrum at the highest p-doping region as reference R_0. The helicity-resolved magnetoreflectance spectra were measured under an out-of-plane magnetic field, by exciting the device with white light of certain helicity and measuring the reflectance of the same helicity.

Calculation of carrier density and electric field. The density of carriers introduced by electrostatic gating is given by $n_e\left(n_p\right) = C_{tg}(V_{tg} - V^0_{tg}) + C_{bg}(V_{bg} - V^0_{bg})$, where C_{tg} (C_{bg}) is the geometry capacitance of the top gate (back gate) and V_{tg} (V_{bg}) is the top-gate (back-gate) voltage. Here V^0_{tg} and V^0_{bg} are the onset gate voltages of the top gate and back gate, respectively, experimentally determined from the regions where moiré excitons peaks X_{II} and X_{III} remain visible (Fig. 1b). The electrical field is given by $E = (V_{tg} - V^0_{tg})/2d_1 - (V_{bg} - V^0_{bg})/2d_2$, where d_1 (d_2) is the thickness of the top (bottom) BN.

MIM measurements. The MIM measurement is performed on a home-built cryogenic scanning probe microscopy platform. A small microwave excitation of about 0.1 mW at a fixed frequency of around 10 GHz is delivered to a chemically etched tungsten tip mounted on a quartz tuning fork. The reflected signal is analysed to extract the demodulated output channels, namely, MIM-Im and MIM-Re, which are proportional to the imaginary and real parts of the admittance between the tip and sample, respectively. To enhance the MIM signal quality, the tip on the tuning fork is excited to oscillate at a frequency of around 32 kHz with an amplitude of approximately 8 nm. The resulting oscillation amplitudes of MIM-Im and MIM-Re are then extracted using a lock-in amplifier to yield d(MIM-Im)/dz and d(MIM-Re)/dz, respectively. The d(MIM)/dz signals are free of fluctuating backgrounds, and their behaviour is very similar to that of standard MIM signals. In this paper, we simply refer to d(MIM)/dz as the MIM signal.

Data availability

Source data are provided with this paper. All other data that support the plots within this paper and other findings of this study are available from the corresponding authors upon reasonable request.

Code availability

The source code for the numerical simulations is available from the corresponding authors upon reasonable request.

Acknowledgements

Z.L. and S.-F.S. acknowledge support from NYSTAR through Focus Center-NY–RPI contract C150117. The device fabrication was supported by the Micro and Nanofabrication Clean Room (MNCR) at Rensselaer Polytechnic Institute (RPI). S.-F.S. also acknowledges support from National Science Foundation (NSF) (Career Grants DMR-1945420 and DMR-2104902) and AFOSR (FA9550-18-1-0312). X.H. and Y.-T.C. acknowledge support from NSF under award DMR-2104805. The optical spectroscopy measurements are also supported by a DURIP award through grant FA9550-20-1-0179. Y.S. and C.Z. acknowledge support from NSF PHY-2110212 and PHY-1806227, ARO (W911NF17-1-0128) and AFOSR (FA9550-20-1-0220). D.C. acknowledges support from the National Natural Science Foundation of China via grant number 62004032. S.T. acknowledges support from DOE-SC0020653, Applied Materials, NSF CMMI 1825594, NSF DMR-1955889, NSF CMMI-1933214, NSF DMR-1904716, NSF 1935994, NSF ECCS 2052527 and DMR 2111812. K.W. and T.T. acknowledge support from the Elemental Strategy Initiative conducted by the MEXT, Japan, via grant number JPMXP0112101001 and JSPS KAKENHI, grant numbers 19H05790 and JP20H00354. L.X. and D.S. acknowledge support from the US Department of Energy (no. DE-FG02-07ER46451) for magnetospectroscopy measurements performed at the National High Magnetic Field Laboratory, which is supported by the NSF through NSF/DMR-1644779 and the State of Florida.

Author contributions

S.-F.S. and Y.-T.C. conceived the project. D.C. and Z.L. fabricated the heterostructure devices and performed the optical spectroscopy measurements. X.H. performed the MIM measurements. M.R. assisted with the device fabrication. M.B. and S.T. grew the TMDC crystals. T.T. and K.W. grew the BN crystals. C.Z. and Y.S. performed the theoretical calculations. L.M., L.Y. and S.-F.S. performed the magnetoreflectance measurements, with the help of L.X. and D.S. S.-F.S., Y.-T.C., C.Z., Y.S., D.C., Z.L., L.M., L.Y. and X.H. analysed the data. S.-F.S. and Y.-T.C. wrote the manuscript with inputs from all the authors.

Competing interests

The authors declare no competing interests.

Additional information

Extended data is available for this paper at https://doi.org/10.1038/s41567-022-01703-y.

Supplementary information The online version contains supplementary material available at https://doi.org/10.1038/s41567-022-01703-y.

Correspondence and requests for materials should be addressed to Zenghui Wang, Chuanwei Zhang, Yong-Tao Cui or Su-Fei Shi.

Peer review information *Nature Physics* thanks Dmitry Efimkin and the other, anonymous, reviewer(s) for their contribution to the peer review of this work.

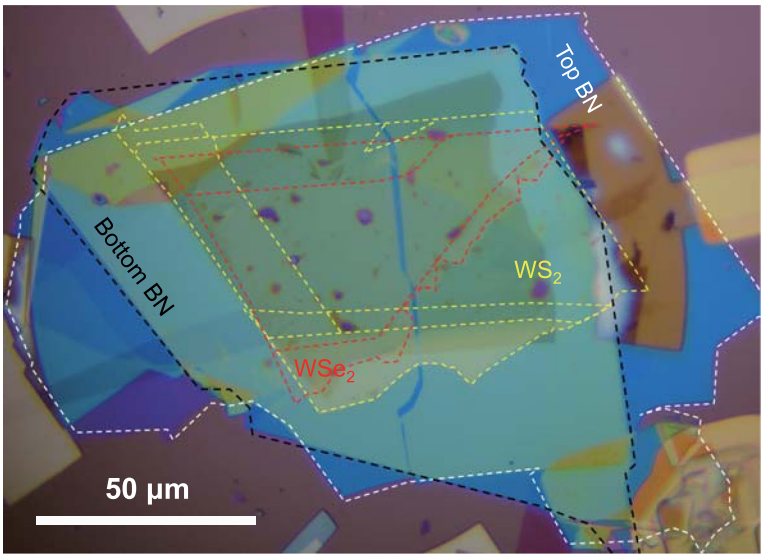

Extended Data Fig. 1 | Optical microscope image of the device D1 presented in the main text.

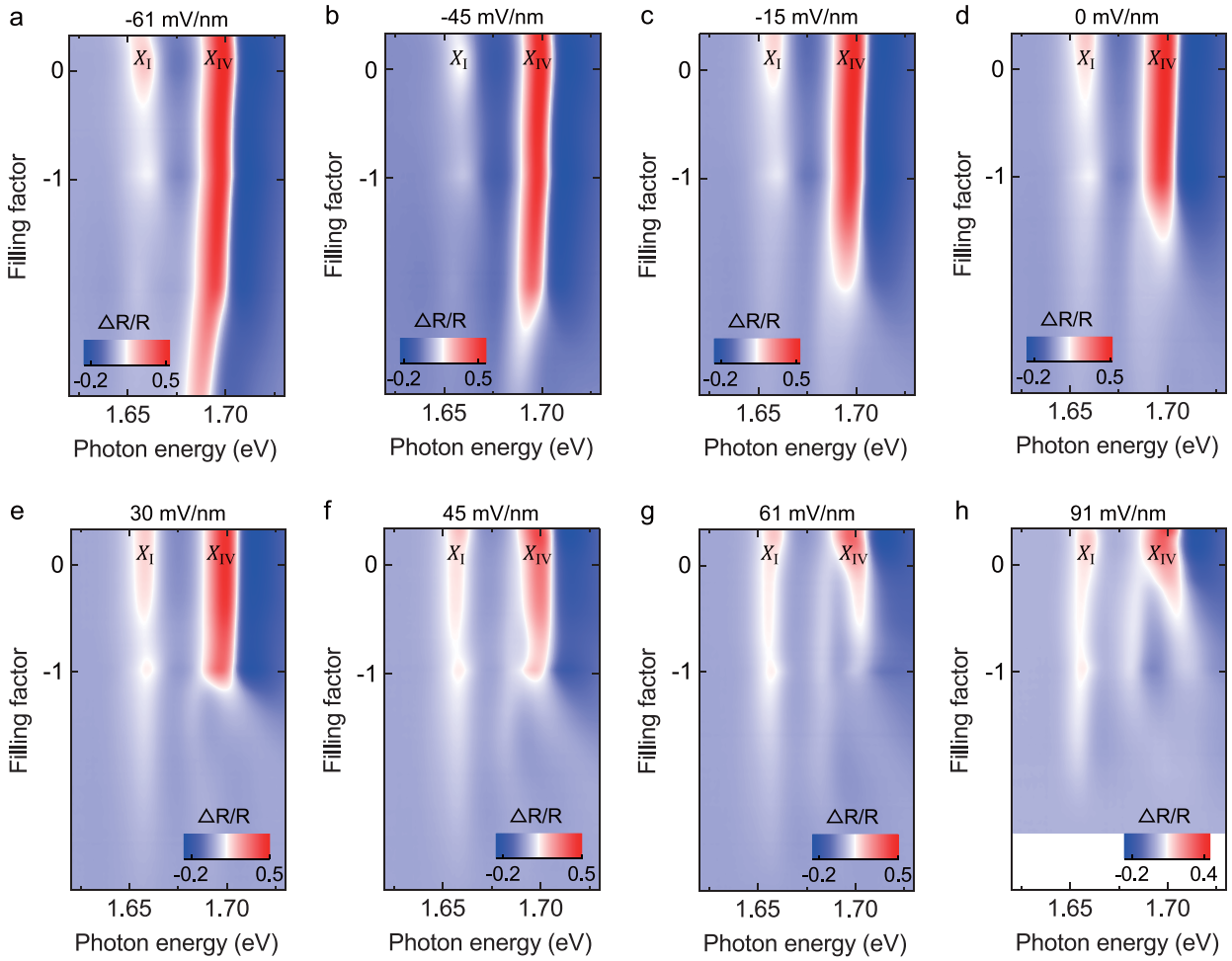

Extended Data Fig. 2 | Electric field tuning of the band alignment in dual-gated 1L/2L WS_2/WSe_2 device D1.

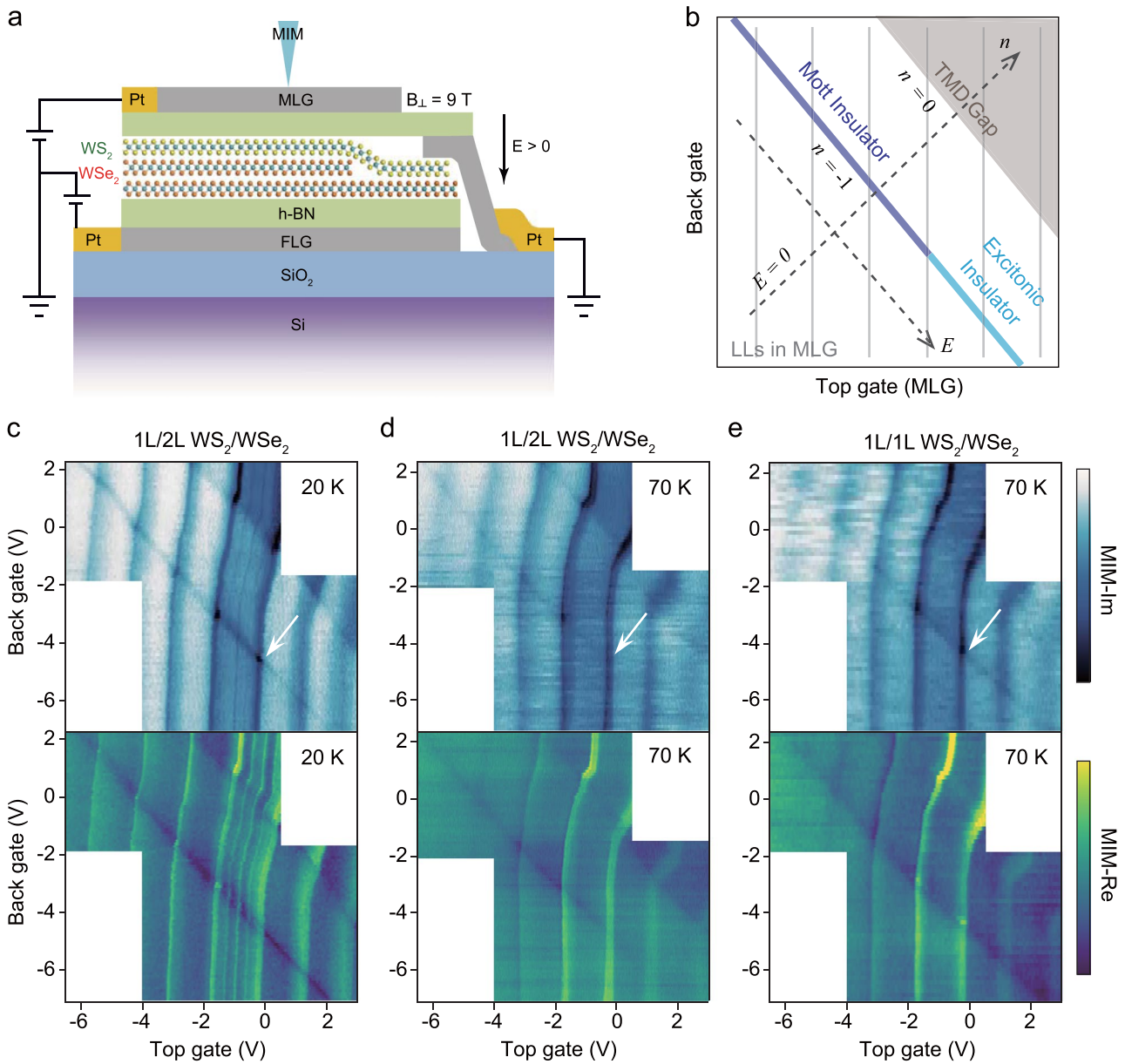

Extended Data Fig. 3 | Transition between Mott insulator and EI states at n = −1 probed by MIM spectra. (a) Schematic of a dual gated 1L/2L WS_2/WSe_2 device D1, same as the device in Fig. 1, but in a region with a monolayer graphene (MLG) as the top gate. **(b)** Schematic of expected MIM features in a dual gate MIM map. **(c)**–(**e**) are color plots of MIM spectra as a function of top gate and back gate voltages for 1L/2L WS_2/WSe_2 region at 20 K (c) and at 70 K (d), and for 1L/1L WS_2/WSe_2 region at 70 K (e), respectively. The top panels are MIM-Im data and the bottom panels are MIM-Re data.

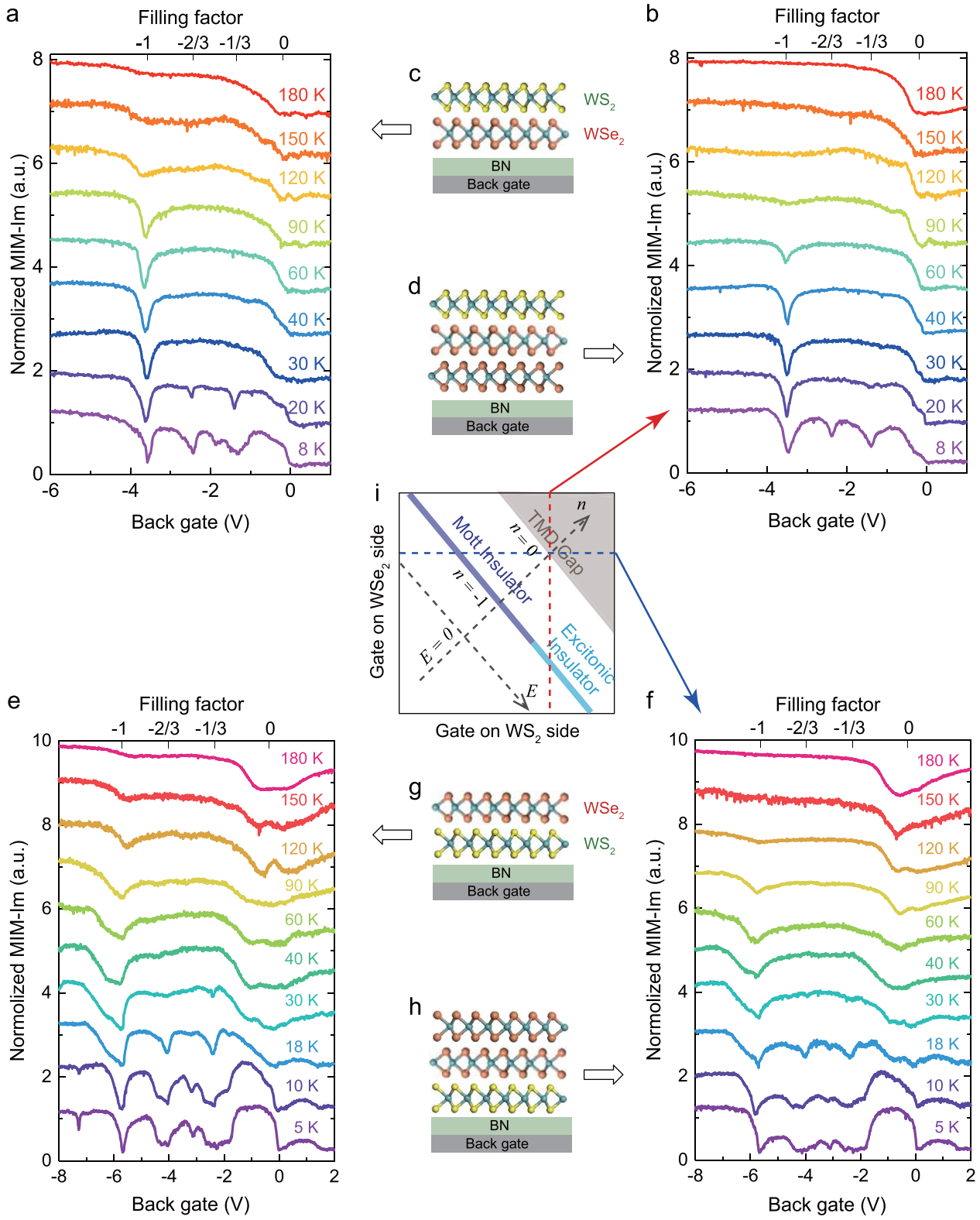

Extended Data Fig. 4 | MIM spectra of single-gated 1L/2L WS_2/WSe_2 devices with opposite stacking orders. (a) MIM spectra as a function of the hole doping for the single gated 1L/1L WS_2/WSe_2 region of device D1, with the device structure schematically shown in **(c)**. (**b**) MIM spectra as a function of the hole doping for the single gated 1L/2L WS_2/WSe_2 region in device D1, with the device stacking order schematically shown in (**d**). (**e**) and (**f**) are doping dependent MIM spectra for the 1L/1L and 2L/1L WSe_2/WS_2 regions in device D5, with the schematic of the stacking shown in (**g**) and **(h)**, respectively. The MIM spectra in **(b)** and **(f)** are equivalent to the red and blue linecuts in the schematic of the dual gate map in (i). Therefore, the n = −1 states in **(b)** and **(f)** correspond to the EI and Mott insulator state, respectively.

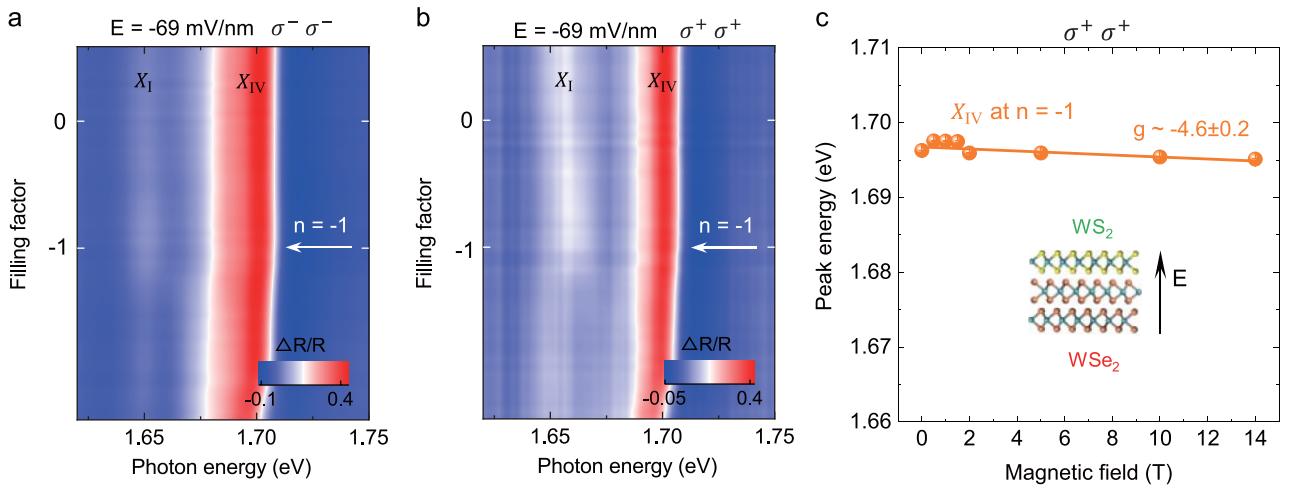

Extended Data Fig. 5 | Magneto-reflectance spectra and Zeeman shifts of the excitons at the Mott insulator state. (a) and (**b**) are helicity-resolved magneto-reflectance spectra of 1L/2L WS_2/WSe_2 region of device D2 as a function of doping for the negative electric field -69 mV/nm, under an out-of-plane magnetic field of 4T. At n = –1, in contrast to Fig. 4, exciton resonance X_{IV}, is evidently A exciton like. (**c**) Zeeman shift of X_{IV} of device D3 at the Mott insulator state (reflectance spectra in Supplementary Fig. 6).